Research article

Epigenomic aberrations of histone methylation in prefrontal cortex of humans with mild cognitive impairment and Alzheimer's disease

Journal of Alzheimer's Disease
1–16

DOI: 10.1177/13872877251414887
journals.sagepub.com/home/alz
Sage | IOS Press

Prachetas Jai Patel[1] and **Zhen Yan**[1,2]

Abstract

Background: Epigenetic mechanisms, particularly histone modifications at gene promoters, are crucial for controlling gene transcription.

Objective: We aim to find out epigenomic aberrations during the progression of neurodegenerative disorders.

Methods: We employed a multifaceted approach to investigate how the two key histone methylation marks, H3K4me3 (linked to gene activation) and H3K27me3 (linked to gene suppression), are altered in postmortem prefrontal cortex of humans with mild cognitive impairment (MCI) or Alzheimer's disease (AD).

Results: Compared to controls, MCI and AD exhibited pronounced losses of permissive H3K4me3 peaks at promoters of genes enriched in synaptic plasticity and neurotransmission, and significant gains of H3K4me3 peaks at promoters of genes enriched in transcriptional regulation. AD displayed more substantial H3K4me3 losses on synaptic genes than MCI. Conversely, significant gains of repressive H3K27me3 peaks were observed at synaptic gene promoters in both disease groups, with MCI exhibiting more pronounced H3K27me3 gains on synaptic genes than AD. Weighted Gene Correlation Network Analysis (WGCNA) revealed multiple modules characterizing distinct patterns of gains and losses of H3K4me3 and H3K27me3 during the transition from MCI to AD. Integrative analysis of epigenomic and transcriptomic data indicated that these histone mark alterations were well correlated with the downregulation of synaptic genes and upregulation of transcriptional regulators in AD.

Conclusions: This comprehensive profiling uncovers a stage-dependent reorganization of histone modifications at critical gene loci, implicating these events in the molecular cascade of AD pathogenesis. Targeting dysregulated chromatin states may offer novel therapeutic avenues for early intervention of AD.

Keywords

Alzheimer's disease, epigenomic, histone methylation, mild cognitive impairment, synaptic genes, transcriptional regulators, transcriptomic

Received: 25 August 2025; accepted: 2 December 2025

Introduction

Alzheimer's disease (AD) is primarily characterized by progressive cognitive decline. Despite extensive research, the mechanisms driving the disease's onset and progression remain elusive, limiting therapeutic interventions primarily to symptom management targeting hallmark pathological features, such as amyloid-beta plaques, tau neurofibrillary tangles, and inflammatory responses.[1,2] Consequently, there is a compelling need to identify underlying molecular events that causally link to AD pathology.

Emerging evidence strongly implicates epigenetic aberrations, particularly histone modification changes, as significant contributors to the aging process and neurodegenerative disorders.[2–6] Histone modifications, such as histone acetylation and methylation, play a critical role in gene transcription through regulating chromatin structure and

---

[1]Department of Physiology and Biophysics, State University of New York (SUNY) at Buffalo, School of Medicine and Biomedical Sciences, Buffalo, NY, USA
[2]VA Western New York Healthcare System, Buffalo, NY, USA

Corresponding author:
Zhen Yan, Department of Physiology and Biophysics, State University of New York (SUNY) at Buffalo, School of Medicine and Biomedical Sciences, 955 Main Street, Buffalo, NY 14203, USA.
Email: zhenyan@buffalo.edu

accessibility, profoundly impacting cellular function.[6–8] While the alteration of histone acetylation in AD has been well documented,[9–13] changes in histone methylation in AD is much less known. The histone H3 trimethylation at lysine 4 (H3K4me3) and at lysine 27 (H3K27me3) is strongly associated with transcriptional activation and repression, respectively.[14,15] However, it is unclear whether these key epigenetic marks are dysregulated in neurodegenerative conditions.

The current study seeks to reveal the alterations in H3K4me3 and H3K27me3 at gene promoters in the prefrontal cortex of humans with mild cognitive impairment (MCI) or AD. MCI is often considered a precursor or a transitional state into AD.[16] Hence, understanding the convergent epigenomic mechanisms in the two disease states could provide significant mechanistic insights.

We implemented a novel integrative strategy combining genome-wide ChIP-seq and Weighted Gene Co-expression Network Analysis (WGCNA) to elucidate co-binding patterns of histone modifications (H3K4me3 and H3K27me3) across promoters during the transition from MCI to AD. This method uniquely reveals how coordinated changes in histone marks contribute to disease progression, a previously unexplored angle in neuroepigenomics.

Furthermore, we integrated epigenomic data with transcriptomic profiles using network-based approaches, thereby elucidating critical molecular pathways that are altered in MCI and AD. Our findings presented herein underscore the significance of epigenomic disruptions in the progression of AD from MCI and highlight histone modifications as promising targets for therapeutic strategies aimed at early intervention and potentially AD prevention.

Methods

Human samples

ChIP-seq data of controls (H3K4me3: n = 13; H3K27me3: n = 12), MCI (H3K4me3 and H3K27me3: n = 11), and AD (H3K4me3 and H3K27me3: n = 17) samples (all females) were acquired from the Rush Alzheimer's Disease Study uploaded on the Encode Project Consortium https://www.encodeproject.org.[17,18] Male samples (Ctrl = 8; MCI = 2; AD = 2) were not included in analyses because of the insufficient sample size and sex-specific differences in histone modifications. All samples were bulk tissues from dorsolateral prefrontal cortex (middle frontal gyrus, BA46). Outliers (2 controls for H3K4me3, 2 controls for H3K27me3) determined by principal component analysis were removed before further analyses. The average age of samples in each group: Ctrl = 86 years; MCI = 90 years; AD = 88 years. Demographic information of the donors is included in Supplemental Table 1.

Data processing and normalization

Raw ChIP-seq peak matrices were processed in Python (v 3.9+), specifically utilizing the Pandas library for data processing and quality control. Normalization of read counts was performed using Post Trimmed Mean of M-values (TMM) normalization implemented via the "edgeR" package,[19] integrated within the "DiffBind" framework (v. 3.16).[20] MCI and AD groups were separately normalized against the same set of controls. Donor postmortem interval and RNA integrity numbers were not available, so we computed a standard set of ChIP-seq QC metrics directly from the BAM files (Supplemental Figure 1).

Differential binding analysis and gene annotation

Differential binding analysis of H3K4me3 and H3K27me3 ChIP-seq data between control and disease groups (MCI or AD) was conducted using the "DiffBind" R package (v. 3.16). Because of the limitation on sample size and data variations, the threshold for significantly changed genomic sites with H3K4me3 or H3K27me3 occupancy was defined as absolute fold change ≥ 1.1 and p values ≤ 0.05, based on the two-sided Wilcoxon "Mann-Whitney" test. Identified differential peaks were annotated to the promoter regions (±3 kb from transcription start sites, TSS) of protein-coding genes using the "ChIPseeker" R package (v.1.42.1). ChIP-seq data were visualized using IGV genome browser. Controls' ChIP-seq data showed similar patterns as publicly available H3K27me3 and H3K4me3 data on human brains.

Gene Ontology (GO) and pathway enrichment analyses

Primary GO enrichment analyses were performed using "EnrichR"[21] for classifying genes with significantly altered H3K4me3 and H3K27me3 occupancy at promoters globally as well as in module eigengenes. They were compared with GO analysis of RNA-seq data. Additionally, synaptic gene enrichments were analyzed using the SYNGO database. Statistical significance was assessed using Fisher's exact test. GO enrichment for ChIP-seq used p-values and for RNA-seq used adjusted p-values.

Protein-protein interaction (PPI) network analysis

PPI networks were constructed using the STRING database[22] (String-db.org), and visualization was performed with "Cytoscape"[23] (v. 3.10.x).

Weighted Gene Correlation Network Analysis

WGCNA was employed to cluster protein-coding genes based on similarity in their binding patterns of H3K4me3 and H3K27me3 across all conditions (Ctrl, MCI, AD), as implemented in the WGCNA R package (v. 1.73).[24] Promoter signals were normalized to library size and stabilized for variance using $\log_2(x+1)$ transformation. Genes with multiple isoforms were summed. Pairwise gene–gene similarity was computed with biweight midcorrelation (cor) across samples. Signed networks with adjacency $a_{\{ij\}} = \left(\frac{1 + cor(x_i,\ x_j)}{2}\right)^{\beta}$ and topological overlap (TOM) for clustering were used. Soft-thresholding powers were chosen by the standard "scale-free topology criterion" (pickSoftThreshold): $\beta = 9$ for H3K4me3 and $\beta = 5$ for H3K27me3, which were the smallest powers achieving $R^2 \approx 0.80$ while maintaining reasonable mean connectivity. Modules were identified with "blockwiseModules" function (signed TOM; minModuleSize = 30; deepSplit = 2 for H3K4me3, 1 for H3K27me3; mergeCutHeight = 0.25) and labeled by the package's arbitrary color scheme. Module eigengenes (MEs) were correlated with traits, and hub genes were ranked by kME (module membership). Genes with significant differential binding (DiffBind) were matched with genes in modules. Networks of significant genes within MEs were visualized in "Cytoscape".

RNA-seq data integration and differential expression analysis

RNA-seq data were extracted from the AD Knowledge Portal (https://adknowledgeportal.org) on the Synapse database (Mayo Clinic and Mount Sinai Brain Bank cohorts of the RNAseq Harmonization Study) via Python. Differentially expressed genes (DEGs) in AD were cross-referenced with differentially bound genes (DBGs) identified from ChIP-seq analyses. Normalized expression counts of selected genes were processed using Python scripts.

Visualization and statistical analyses

Principal component analysis (PCA) and MA plots for ChIP-seq data were generated in R. Ridge plots depicting distributions of ChIP-seq peaks were created using the "ggridges" package (v.0.5.6), along with supporting packages (grid v.4.4.2 and ggplot2 v.3.5.2).

MA Plots of ChIP binding data from "DiffBind", Boxplots and violin plots of RNA-seq, Microarray and ChIP-seq binding scores were generated using residualized count data (RNA-seq), normalized expression (Microarray) and normalized binding scores (ChIP) processed via Python and visualized using R (ggplot2). Statistical comparisons between groups for boxplots were conducted using the two-sided Wilcoxon "Mann-Whitney" test, Kruskal-Wallis test, or Wilcoxon signed-rank test, as specified. ANOVA was used to compare the correlation coefficients of MEs-disease relationship box plots.

Results

H3K4me3 occupancies are lost on synaptic genes and gained on transcription regulators in both MCI and AD

H3K4me3 ChIP-seq data were examined in 11 MCI, 17 AD, and 11 age-matched control samples with no cognitive impairment. As shown in the PCA plots (Figure 1A), the diseased groups were largely segregated from controls in the sample distribution of H3K4me3 peaks. Differential binding analysis identified many significantly changed genomic sites with H3K4me3 occupancy (MCI: 4368; AD: 3319). Filtering and limiting to the promoter region (+/- 3 kb of TSS) of protein-coding genes, MCI had significant H3K4me3 gains on 436 sites (407 genes) and losses on 720 sites (698 genes), while AD had significant H3K4me3 gains on 564 sites (534 genes) and losses on 702 sites (701 genes) (Figure 1B, Supplemental Table 2).

Using Gene Set Enrichment analysis (GSEA), we examined Gene Ontology (GO) pathways of these genes with significant changes in H3K4me3 binding at promoters. As shown in Figure 1C, genes with H3K4me3 losses in MCI and AD were enriched in synapse organization and synapse transmission; while genes with H3K4me3 gains in MCI and AD were enriched in RNA polymerase II-mediated transcription.

SYNGO analysis (Figure 1D) revealed that, in MCI, the 94 synaptic genes with H3K4me3 losses were enriched in postsynaptic density, while in AD, the 119 synaptic genes with H3K4me3 losses were enriched in both postsynaptic and presynaptic sites. AD displayed more substantial H3K4me3 losses on synaptic genes than MCI.

We also generated protein-protein interaction (PPI) networks of hub genes with changed H3K4me3 in MCI and AD. For top 20 synaptic hub genes with H3K4me3 losses, MCI had voltage-gated calcium channels (VDCC) (*CACNG3* and *CACNA1A*), synaptic plasticity molecule CaMKII (*CAMK2A*), and cytoskeleton regulators Alpha-actinin-1 (*ACTN1*) and Talin-2 (*TLN2*); while AD had VDCC (*CACNG3* and *CACNG2*), synaptic organizer neurexin-1 (*NRXN1*), glutamate receptors (*GRIK2* and *GRIA2*), and synaptogamins (*SYT1* and *SYT4*) that act as Ca^{2+} sensors for neurotransmitter release (Figure 1E). For the top 20 transcriptional hub genes with H3K4me3 gains, MCI had transcription factors and regulators, such as *RUNX3, GATA3*, *FOXP1*, *OTX2*, *PITX2*, *ZEB2*, *MEIS1, EZH2*, *PRDM14*, and *PIK3R1,* while AD had transcription factors, including *RUNX3, GATA3, FOXA2*, *OTX2*, *SMAD3*, *NEUROD1* and *PAX2/5/8* (Figure 1F).

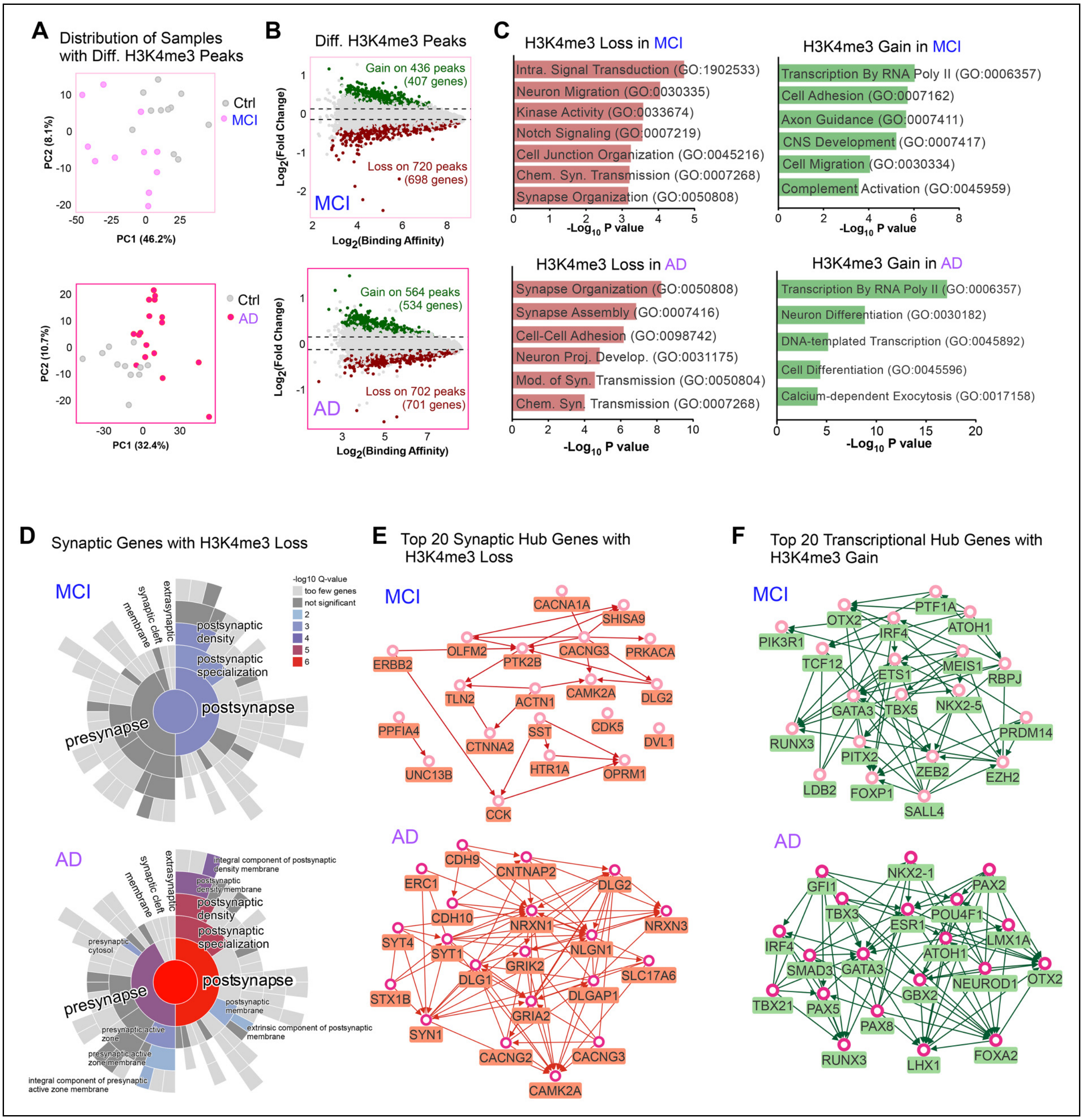

Figure 1. H3K4me3 alterations in MCI and AD. (A) PCA plots depicting H3K4me3 peaks' sample distribution in control (Ctrl) versus MCI (top) or Ctrl versus AD (bottom). Ctrl: n = 13; MCI: n = 11; AD: n = 17. (B) MA plots depicting differential H3K4me3 binding scores in MCI (top) and AD (below), compared to Ctrl. Significant gains (green) and losses (red) are also labeled. P values were calculated using a two-sided Wilcoxon "Mann-Whitney" test. (C) Gene Ontology (GO) of protein-coding genes with significant H3K4me3 losses (left) or gains (right) at their promoters in MCI (top) and AD (bottom). P values were calculated using Fisher's Exact test. (D) SYNGO cellular component analysis of synaptic genes with significant H3K4me3 losses in MCI (top) and AD (bottom). P values were calculated using Fisher's Exact test. (E) PPI of top 20 synaptic hub genes with H3K4me3 losses in MCI (top) and AD (bottom). (F) PPI of top 20 transcriptional hub genes with H3K4me3 gains in MCI (top) and AD (bottom).

Module eigengenes with correlated H3K4me3 binding show disease-specific H3K4me3 losses and gains

WGCNA segregated protein-coding genes with H3K4me3 binding at their promoters into 12 module eigengenes (MEs) (Figure 2A) based on similarity in binding patterns. These MEs were sorted according to their sizes, and the percentage of genes with differential H3K4me3 binding in MCI and AD (compared to controls) in each ME is shown in Figure 2B (Supplemental Table 3). Three modules were selected for more detailed analyses.

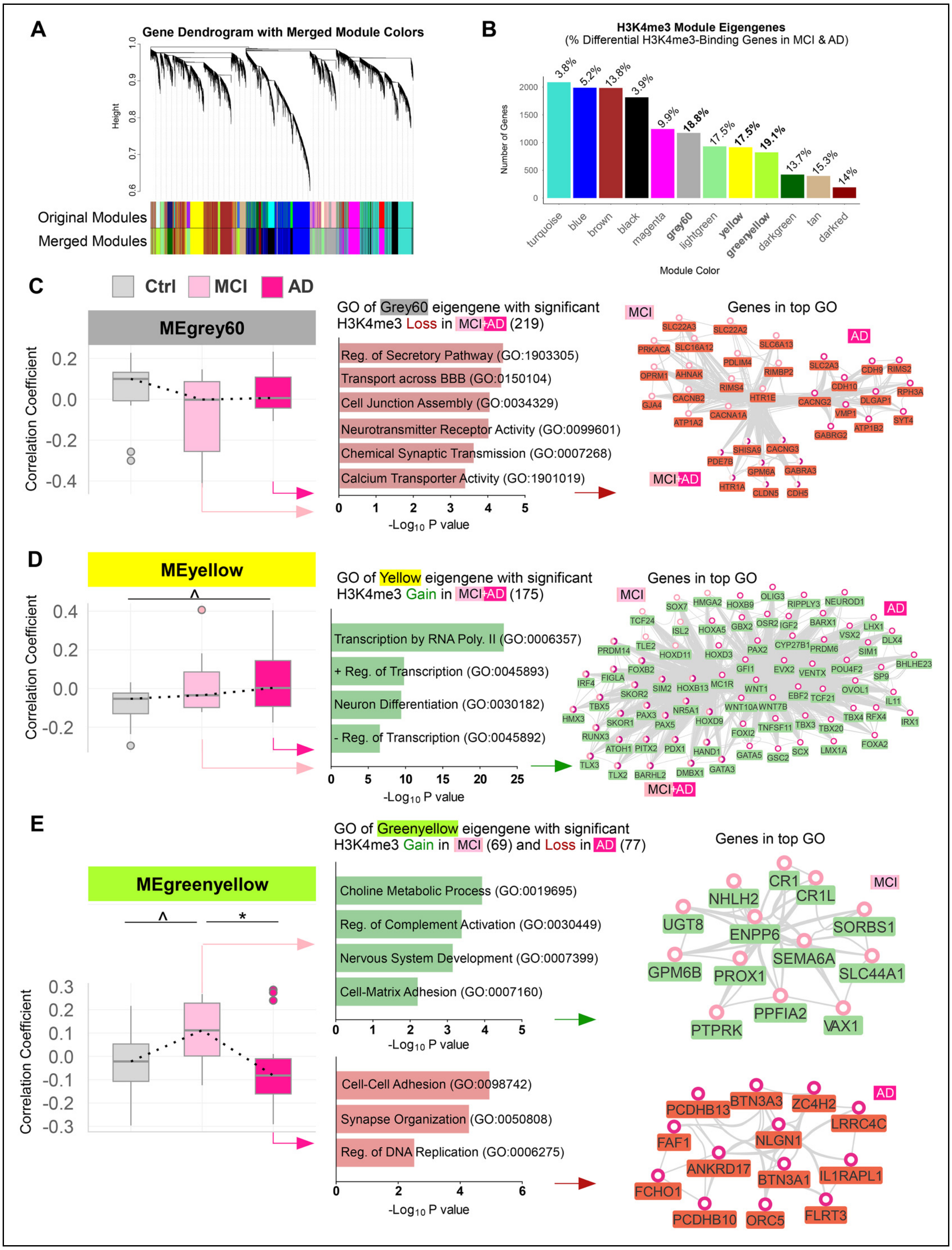

Figure 2. H3K4me3 losses and gains in module eigengenes with correlated H3K4me3 binding in MCI and AD. (A) Dendrogram depicting protein-coding genes with H3K4me3 binding at their promoters clustered into module eigengenes (MEs) using weighted similarity scores derived from positive correlations from all 3 groups (Ctrl, MCI, AD). Ctrl: n = 11; MCI: n = 11; AD: n = 17. Modules were assigned to a random color and consolidated using a set threshold. (B) H3K4me3 MEs sorted according to size. The percentage of genes with significant ($p \leq 0.05$) H3K4me3 changes in each module is also labeled. P values were calculated using Weighted Fisher test to consolidate gene isoforms and two-sided Wilcoxon "Mann-Whitney" test for individual genes. (C, F, I) Box plots of correlation coefficient between H3K4me3 module eigengenes (C: MEgrey60, F: MEyellow, I: MEgreenyellow) and patient conditions (Ctrl, MCI, AD). Significant differences in correlation coefficient magnitude: MEgrey60: $p = 0.19$, MEyellow: $p = 0.099$, MEgreenyellow: $p = 0.038$, one-way ANOVA with *post hoc* analysis, * $p_{adj.} \leq 0.05$, ^ $p_{adj.} \leq 0.2$. (D, G, J) GO of MEgrey60 with significant H3K4me3 losses in MCI and AD (D), MEyellow with significant H3K4me3 gains in MCI and AD (G) and MEgreenyellow with significant H3K4me3 gains in MCI and losses in AD (J). (E, H, K) PPI of MEgrey60 (E), MEyellow (H) and MEgreenyellow (K) in top GO with significant H3K4me3 losses or gains in MCI and AD.

MEgrey60 (1173 genes) represented the module of "Synaptic Transmission and Ion Homeostasis Regulation" and demonstrated a lower correlation coefficient magnitude of H3K4me3 binding in MCI and AD, compared to controls (Figure 2C). 219 genes within MEgrey60 were determined to be differentially bound genes (DBGs) by DiffBind. Significant H3K4me3 losses in MCI and AD were enriched in regulation of secretory pathway, neurotransmitter receptor activity and chemical synapse transmission (Figure 2D). PPI network of these genes in top GO (Figure 2E) included VDCC (*CACNAG3/2, CACNA1A*, *CACNB2*), synaptic membrane transporters (*SLCA6A13*, *SLC16A12*, *SLC22A2/3)*, exocytosis regulators (*RIMS4/2*, *RIMBP2, SYT4)*, and cadherins (*CDH5/9/10).*

MEyellow (916 genes) represented the module of "Transcriptional Regulation of Neurogenesis and Inflammatory Signaling" and the module-disease relationship trended towards an increased correlation coefficient of H3K4me3 binding in MCI and AD (Figure 2F). 175 DBGs in MEyellow with significant H3K4me3 gains in MCI and AD were enriched in RNA polymerase II-mediated transcription, positive and negative regulation of transcription, and neuron differentiation (Figure 2G). PPI network of these genes in top GO (Figure 2H) included transcription factors *RUNX3*, *FOXB2*, *SOX7*, *HOXA5*, *HOXB9*, *HOXD3/9/11, PAX2/3/5*, etc.

MEgreenyellow (824 genes) represented the module of "Cell Adhesion and Synaptic Organization in Neural Development" and trended towards an increased correlation coefficient of H3K4me3 binding in MCI followed by a downward trend in AD (Figure 2I). The 69 DBGs within MEgreenyellow with significant H3K4me3 gains in MCI were enriched in choline metabolic process (*UGT8* and *ENPP6)*, regulation of complement activation (*CR1*, *CR1L)*, nervous system development (*PTPRK*, *PPFIA2)* and cell-matrix adhesion (*GPM6B* and *SEMA6A)* (Figure 2J and 2K, top). The 77 DBGs within MEgreenyellow with significant H3K4me3 losses in AD were enriched in cell-cell adhesion (PCDHB*10/13)* and synapse organization (*NLGN1, LRRC4C*) (Figure 2J and 2K, bottom).

A few other modules also showed differing patterns in module-disease relationships of H3K4me3 binding (Supplemental Figure 2). These included MEblue (1989 genes: "Transcriptional and Phosphorylation-Dependent Regulation of Developmental Signaling"), MEmagenta (1244 genes: "Nuclear and Mitochondrial Gene Expression Machinery Biogenesis"), MElightgreen (931 genes: "Regulation of Synaptic Signaling and Intracellular Signal Transduction Pathways"), and MEdarkgreen (423 genes: "Regulation of GTPase Signaling and Synaptic Communication"). MEblue had 47 DBGs involved in apoptotic process and 5 genes involved in immune response with increased H3K4me3 binding in MCI.

H3K27me3 occupancies are gained on synaptic genes in both MCI and AD

In addition to the permissive H3K4me3, we next examined repressive H3K27me3 ChIP-seq data in control, MCI and AD. Segregation between diseased groups and controls in the sample distribution of H3K27me3 peaks was shown in PCA plots (Figure 3A). Differential analysis revealed 6650 significantly altered H3K27me3 binding sites in MCI, with much more gains (944 peaks, 844 genes) than losses (233 peaks, 217 genes) at the promoter of protein-coding genes. Similarly, in AD, 6035 changed H3K27me3 binding sites were identified with much more gains (704 peaks, 641 genes) than losses (165 peaks, 159 genes) at promoters of protein-coding genes (Figure 3B, Supplemental Table 4).

In both MCI and AD, genes with significant H3K27me3 gains were enriched in chemical synapse transmission, cation transmembrane transport, and neurotransmitter receptor activity (Figure 3C). SYNGO (Figure 3D) revealed that the 147 synaptic genes with H3K27me3 gains in MCI were enriched in postsynaptic and presynaptic membranes, while the 87 synaptic genes with H3K27me3 gains in AD were mainly enriched in postsynaptic specializations. MCI exhibited more pronounced H3K27me3 gains on synaptic genes than AD.

As shown in PPI networks of top 20 synaptic hub genes with H3K27me3 gains (Figure 3E), MCI had VDCC (*CACNG3/5/8*), glutamate synapse molecules (*GRIN2D*, *GRIN2C*, *SHANK1*/2, *GRM5, DLG2*), and growth factors (*BDNF, IGF1, EGFR*); while AD also had VDCC (*CACNG3/8, CACNA1A*), glutamate synapse molecules (*GRIN1*, *GRIK3*, *SHANK1/2/3*), and vesicle exocytosis regulators (SYN1/2, *UNC13A* and *CPLX1*).

Module eigengenes with correlated H3K27me3 binding show disease-associated H3K27me3 gains

We further performed WGCNA analyses of module eigengenes with H3K27me3 binding (Figure 4A). Modules with the most significantly changed genes revealed from differential analysis were picked for further analysis (Figure 4B, Supplemental Table 5).

MEblack (862 genes) represented one module of "Synaptic Signaling and Neuronal Ion Transport" and showed a trend of increased positive correlation coefficient of H3K27me3 binding in MCI, but not in AD (Figure 4C). 210 corresponding DBGs in MEblack with significant H3K27me3 gains in MCI were enriched in chloride transport, chemical synaptic transmission, cell-cell adhesion, synapse organization, and synaptic transmission (Figure 4D). These genes in top GO (Figure 4E) included *CACNG3*, *GABRA1/3*, *DLG2*, *SLC1A1/7*, *SLC8A3*, and *PCDHGC3*.

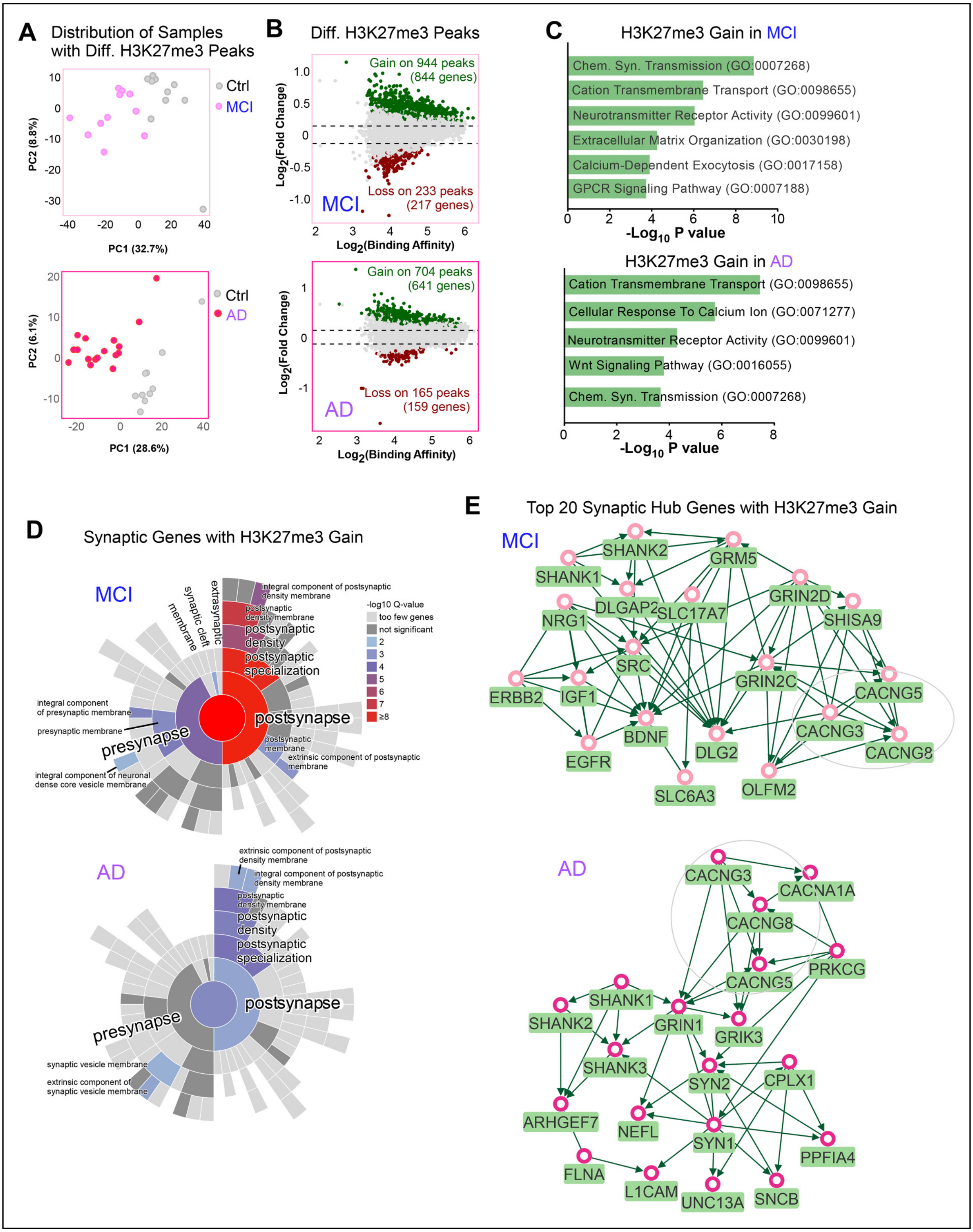

Figure 3. H3K27me3 alterations in MCI and AD. (A) PCA plots depicting H3K27me3 peaks' sample distribution in Ctrl versus MCI (top) or Ctrl versus AD (bottom). Ctrl: n = 10; MCI: n = 11; AD: n = 17. (B) MA plots depicting differential H3K27me3 binding scores in MCI (top) and AD (below), compared to Ctrl. Significant gains (green) and losses (red) are also labeled. P values were calculated using a two-sided Wilcoxon "Mann-Whitney" test, with a threshold of ≤ 0.05. (C) GO of protein-coding genes with significant H3K27me3 gains at their promoters in MCI (top) and AD (bottom). P values were calculated using Fisher's Exact test. (D) SYNGO cellular component analysis of synaptic genes with significant H3K27me3 gains in MCI (top) and AD (bottom). P values were calculated using Fisher's Exact test. (E) PPI of top 20 synaptic hub genes with H3K27me3 gains in MCI (top) and AD (bottom).

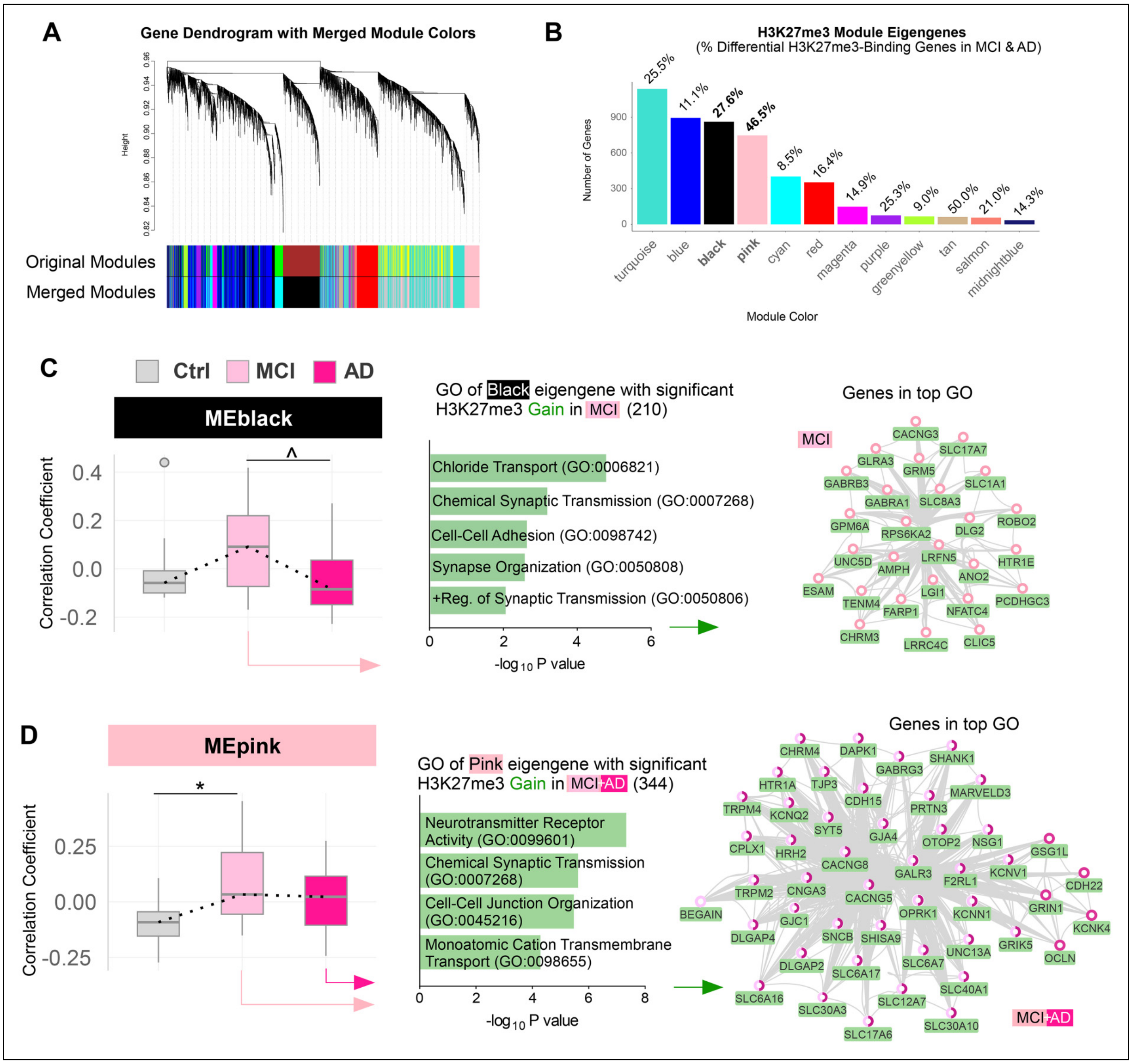

Figure 4. H3K27me3 gains in module eigengenes with correlated H3K27me3 binding in MCI and AD. (A) Dendrogram depicting protein-coding genes with H3K27me3 binding at their promoters clustered into module eigengenes (MEs) using weighted similarity scores derived from positive correlations from all 3 groups (Ctrl, MCI, AD). Ctrl: n = 10; MCI: n = 11; AD: n = 17. (B) H3K27me3 MEs sorted according to size. The percentage of genes with significant ($p \leq 0.05$) H3K27me3 changes in each module is also labeled. P values were calculated using Weighted Fisher test to consolidate gene isoforms and two-sided Wilcoxon "Mann-Whitney" test for individual genes. (C, F) Box plots of correlation coefficient between H3K27me3 module eigengenes (C: MEblack; F: MEpink) and patient conditions (Ctrl, MCI, AD). Significant differences in correlation coefficient magnitude: MEblack: $p = 0.12$, MEpink: $p = 0.045$, one-way ANOVA with *post hoc* analysis, * $p_{adj.} \leq 0.05$, ^ $p_{adj.} \leq 0.2$. (D, G) GO of MEblack with significant H3K27me3 gains in MCI (D) and MEpink with significant H3K27me3 gains in MCI and AD (G). (E, H) PPI of MEblack (E) and MEpink(H) in top GO with significant H3K27me3 gains in MCI and AD.

MEpink (747 genes) represented another module of "Synaptic Signaling and Neuronal Ion Transport" and showed a trend of increased H3K27me3 binding in both MCI and AD (Figure 4F). The corresponding 344 DBGs within MEpink with significant H3K27me3 gains in MCI and AD were enriched in neurotransmitter receptor activity, chemical synapse transmission, cell-cell junction organization (Figure 4G). These genes in top GO (Figure 4H) included *CACNG5/8, GABRG3, SHANK1, SYT5, GRIK5,* etc.

A few other modules also showed differing patterns in module-disease relationships of H3K27me3 binding (Supplemental Figure 3). MEturquoise (1138 genes: "Wnt Signaling and Transcriptional Regulation of Neuronal Differentiation") had a significant increase of H3K27me3 binding on genes related to development and cell proliferation. MEblue (894 genes: "Immune Defense Signaling and Leukocyte Chemotaxis ") had 4 cytokine-related DBGs with significant increase of H3K27me3 binding in MCI. MEred (353 genes: "GPCR-Mediated Signaling and Transcriptional Control of Cell Migration ") had 7 DBGs related to cell proliferation and 4 DBGs related to programmed cell death with significantly increased H3K27me3 binding in AD.

MCI and AD have shared and unique alterations of H3K4me3 and H3K27me3

Next, we compared the alterations of histone modifications that are common or unique in MCI and AD. As shown in Figure 5A, among genes with H3K4me3 losses, 11% (136 genes) were shared and 45% (565 genes) were AD-specific, both of which were enriched in cell junction assembly and synapse organization; while 44% (562 genes) were unique to MCI, which were related to apoptosis, cell migration, and stress response, suggesting early disruption of cellular homeostasis. For genes with H3K4me3 gains (Figure 5B), 14% (116 genes) were common, 51% (418 genes) were AD-specific, and 35% (291 genes) were unique to MCI, all of which were enriched in transcriptional regulation. For genes with H3K27me3 gains (Figure 5C), 26% (290 genes) were shared, 29% (325 genes) were AD-specific, and 45% (385 genes) were unique to MCI, all of which were enriched in synaptic transmission and neurotransmitter/ion transport. In addition, genes with MCI-specific H3K27me3 gains were involved in protein tyrosine kinase signaling and MAPK cascade, while genes with AD-specific H3K27me3 gains were involved in dopaminergic neuron differentiation and Wnt signaling.

Transcriptomic changes in AD are correlated with H3K4me3 and H3K27me3 alterations

Given the alteration of H3K4me3 (linked to gene activation) and H3K27me3 (linked to gene repression) in AD, we examined its potential link to transcriptomic changes. Using the RNA-seq data from two large scale studies (Mayo Clinic and Mount Sinai Brain Bank combined), we found that downregulated genes in AD were enriched in chemical synapse transmission (Figure 6A, top), similar to the GO categories of genes with significant H3K4me3 losses and H3K27me3 gains in AD (Figures 1C and 3C). On the other hand, upregulated genes in AD were enriched in regulation of DNA-templated transcription (Figure 6A, bottom), similar to the GO categories of genes with significant H3K4me3 gains (Figure 1C).

Among the 1884 downregulated genes in AD (Mayo), 201 genes had significant H3K4me3 losses and 220 genes had significant H3K27me3 gains in MCI or AD, 36 genes showed all the three changes (transcriptional down, H3K4me3 loss, H3K27me3 gain) (Figure 6B, top left), 18 of which were synaptic genes including *CACNG3* (VDCC) (Figure 6B, top right, Supplemental Table 7).

On the other hand, among the 2155 upregulated genes in AD (Mayo), 124 genes had significant H3K4me3 gains in MCI or AD (Figure 6B, bottom left). These genes were highly enriched in DNA-templated transcription regulation, including *RUNX3* (transcription factor) (Figure 6B, bottom right, Supplemental Table 7).

We selected *CACNG3* and *RUNX3* for further analysis. As shown in the representative ChIP-seq landscape plots (Figure 6C), in both MCI and AD, H3K4me3 peaks at *CACNG3* promoter were markedly reduced, and H3K27me3 peaks at *CACNG3* promoter were pronouncedly increased. Statistical analyses of all samples revealed the significant loss of permissive H3K4me3 binding and gain of repressive H3K27me3 binding on *CACNG3* in MCI and AD (Figure 6D), correlated with the significant reduction of *CACNG3* mRNA expression in AD by RNA-seq and microarray studies (Figure 6E). Similarly, ChIP-seq also showed significantly increased H3K4me3 binding at *RUNX3* promoter (Figure 6F, G), which was correlated with the significantly increased *RUNX3* mRNA expression in AD from RNA-seq and microarray data (Figure 6H).

Discussion

We propose a model demonstrating significant alterations of histone methylation landscapes in the prefrontal cortex during the progression from MCI to AD, which may contribute to transcriptional dysregulation, synaptic loss, and cognitive impairment (Figure 7). Specifically, we identified robust reductions of permissive H3K4me3 and concomitant increases of repressive H3K27me3 marks at promoters of synaptic genes, accompanied by heightened H3K4me3 occupancies at transcriptional regulators. These findings suggest a coordinated epigenomic reorganization that underlies synaptic dysfunction, a hallmark of AD pathology.[25–27]

In both MCI and AD, synaptic genes, such as *CACNG3, SYT5, NRXN1, GRIA2, GABRG3,* and *GRIK2,* exhibit diminished H3K4me3 and increased H3K27me3, which synergistically reduces their transcription, leading to the impaired neuronal plasticity, neurotransmitter signaling, and cognitive function.[28,29] As shown in one example, *CACNG3* (a VDCC subunit), its pronounced H3K4me3 depletion and robust H3K27me3 enrichment in MCI and AD correlate strongly with transcriptional downregulation in AD. Dysfunction of VDCCs, particularly CACNG subunits, disrupts calcium homeostasis critical for synaptic plasticity, memory formation, and neuronal survival.[30,31] Thus, epigenetic suppression of *CACNG3* could directly contribute to synaptic dysfunction in AD pathogenesis.

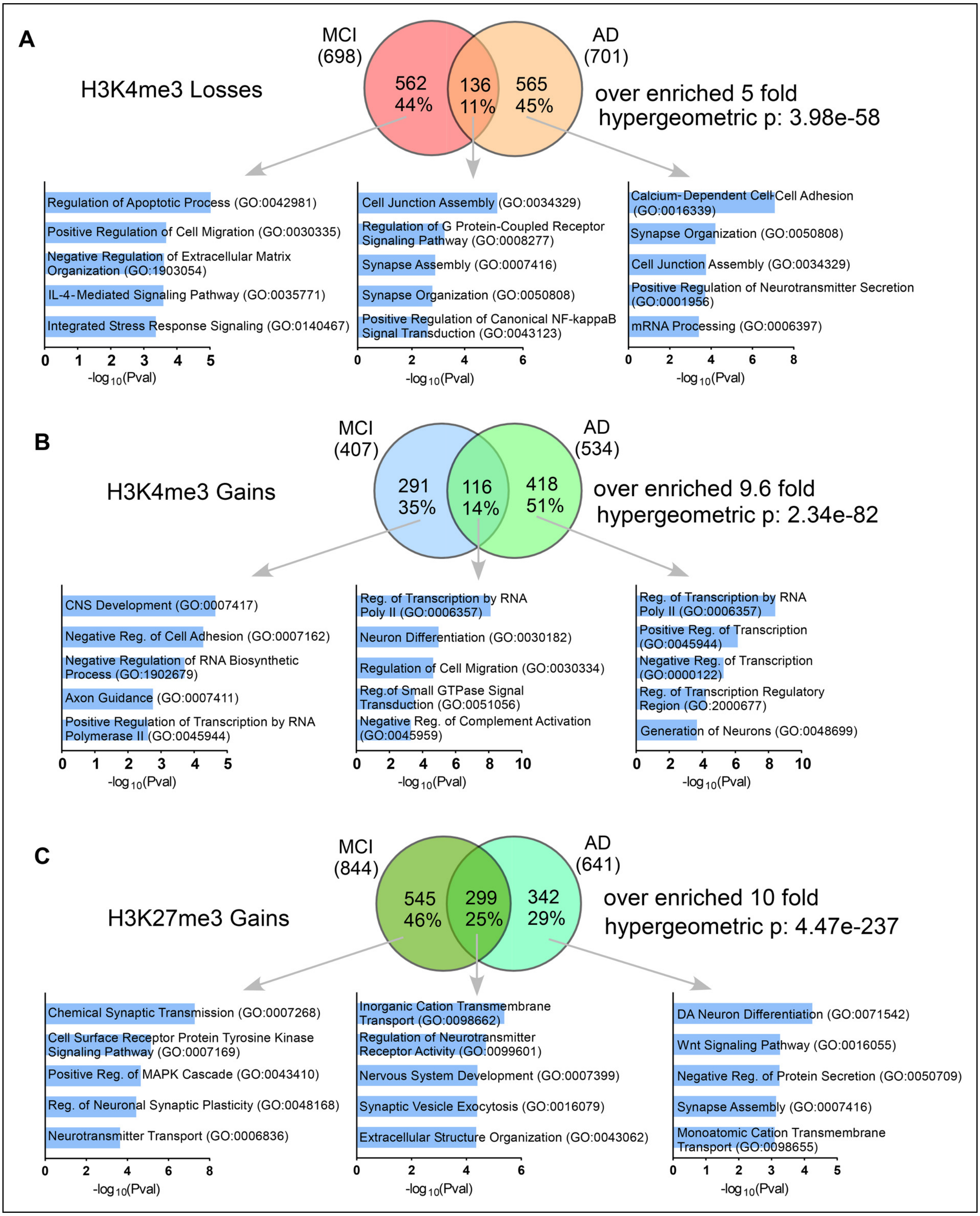

Figure 5. MCI and AD have common and unique alterations of histone modifications. (A-C) Venn diagrams illustrating the overlapped and distinct genes with significant H3K4me3 losses (A), H3K4me3 gains (B), or H3K27me3 gains (C) in MCI and AD. Percentages within each circle indicate the proportion of genes unique to each condition or shared between them. The associated bar plots show representative Gene Ontology (GO) biological processes enriched in each category.

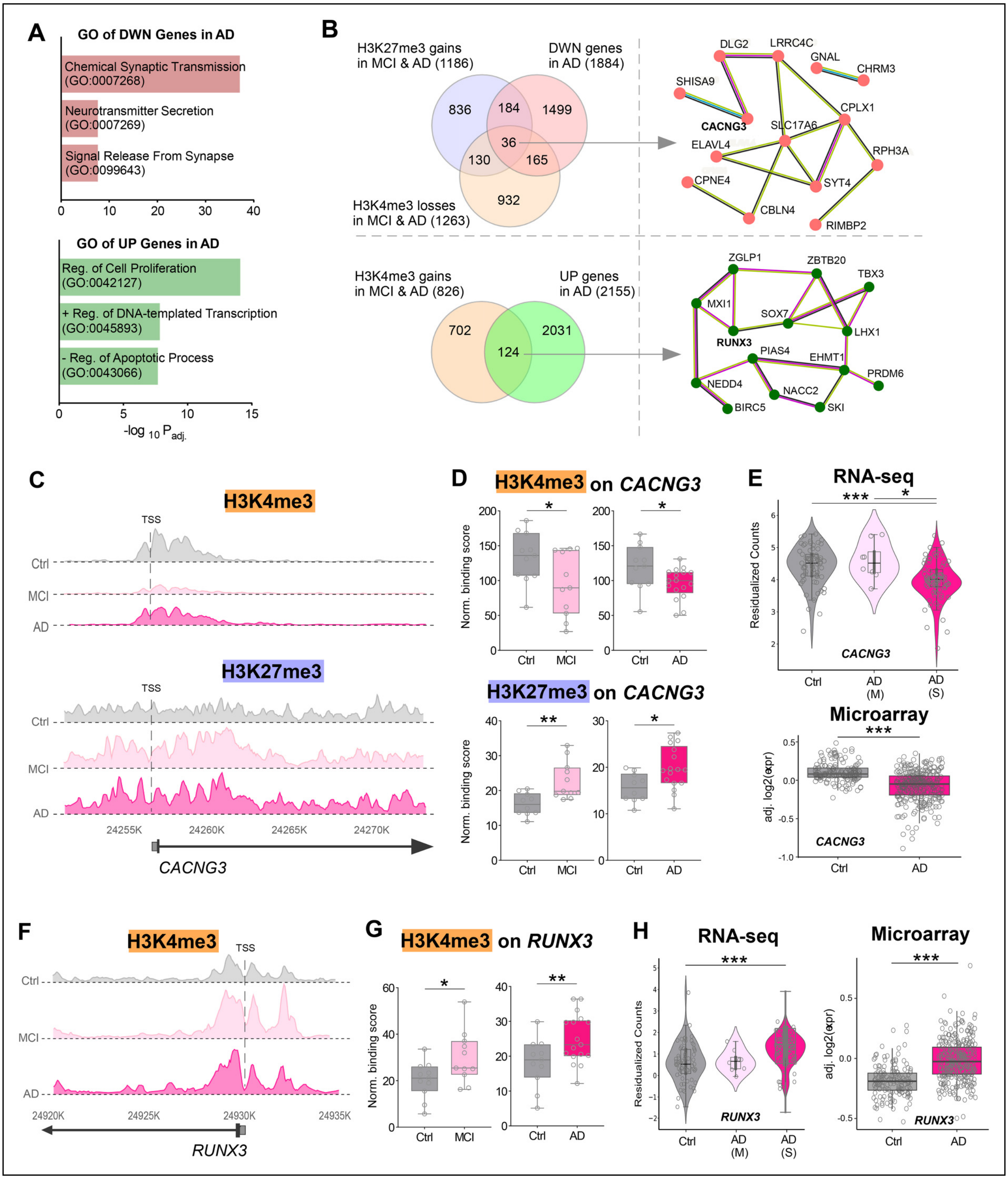

Figure 6. Correlation of transcriptomic changes in AD with H3K4me3 and H3K27me3 alterations. (A) GO of differentially expressed genes in AD commonly found from two large-scale RNA-seq studies (Mayo Clinic and Mount Sinai). Top: GO of downregulated genes in AD; Bottom: GO of upregulated genes in AD. Adjusted p values were calculated using Fisher's Exact Test. (B) Venn diagrams depicting common genes with mRNA downregulation, H3K4me3 losses and H3K27me3 gains in MCI and AD (top left), or genes with significant mRNA upregulation and H3K4me3 gains in MCI and AD (bottom left), as well as PPI of the common synaptic genes (top right) or transcriptional regulators (bottom right). (C, F) ChIP-seq landscapes showing H3K4me3 and H3K27me3 peaks at *CACNG3* promoter (C) or H3K4me3 peaks at *RUNX3* promoter (F) in representative Ctrl, MCI and AD samples. (D, G) Box plots showing H3K4me3 and H3K27me3 binding scores on *CACNG3* (H3K4me3, MCI: $p = 0.038$, AD: $p = 0.020$; H3K27me3, MCI: $p = 0.002$, AD: $p = 0.021$; Wilcoxon "Mann-Whitney" test) (D) or H3K4me3 binding scores on *RUNX3* (MCI: $p = 0.010$, AD: $p = 0.005$) (G) in all Ctrl, MCI and AD samples. (E, H) Violin and box plots of RNA-seq or microarray data showing *CACNG3* (E) or *RUNX3* (H) mRNA expression in Ctrl, moderate (M) AD or severe (S) AD groups (RNA-seq, *CACNG3*: $p = 1.69e\text{-}05$, *RUNX3*: $p = 1.01e\text{-}04$, Kruskal-Wallis test; Microarray, *CACNG3*: $p = 2.2e\text{-}16$, *RUNX3*: $p = 2.2e\text{-}16$, Wilcoxon signed-rank test).

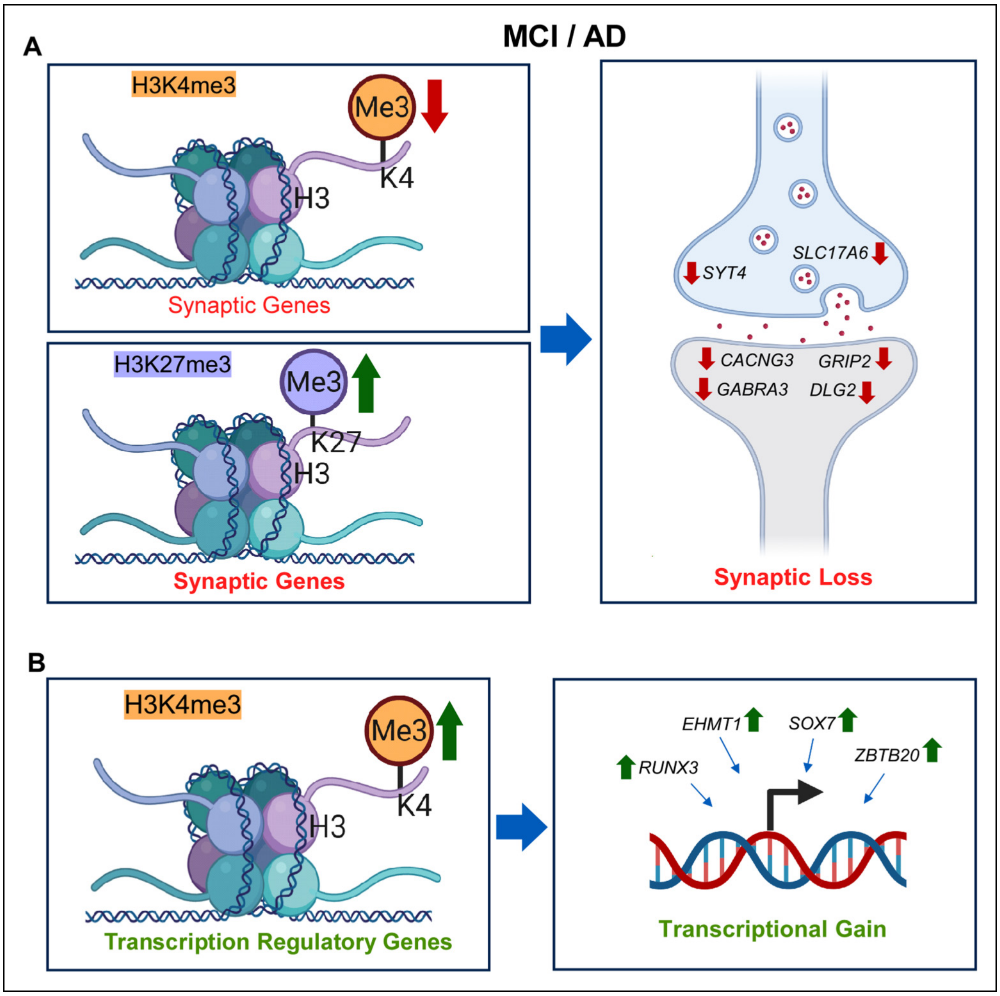

Figure 7. A schematic model of epigenomic changes and consequences in MCI and AD. (A) The loss of permissive H3K4me3 and gain of repressive H3K27me3 on synaptic genes in MCI and AD are correlated with the reduced expression of synaptic genes and diminished synaptic function. (B) The gain of permissive H3K4me3 on transcription regulatory genes in MCI and AD is associated with the excessive transcriptional activity and aberrant gene regulation.

Our findings align well with a genome-wide characterizations of histone methylation in AD brains, which showed a loss of H3K4me3 at genes critical for synaptic function.[32] Given that different AD samples were used in both studies, it suggests that H3K4me3 occupancy is lost at synaptic genes regardless of sex, age or brain region differences. Interestingly, familial AD models also show altered histone methylation, predominantly H3K4me3 losses at neuronal identity genes and H3K27me3 gains at synaptic loci.[33] These changes closely mirror our findings in sporadic AD, suggesting a unified epigenetic vulnerability potentially driving cognitive decline irrespective of genetic etiology.

In parallel, we observed significant increases of H3K4me3 occupancies at promoters of transcriptional regulators, such as *RUNX3, EZH2, OTX2, GATA3,* and *PAX5*, leading to elevated transcriptional activity. These transcription factors orchestrate cellular responses, including DNA repair, neuronal differentiation, and inflammation.[34–36] As shown in one example, *RUNX3,* its increased H3K4me3 occupancy in MCI and AD correlate strongly with transcriptional upregulation in AD. RUNX family transcription factors have been recognized as neuroprotective modulators that enhance DNA repair and survival pathways in neurodegenerative contexts.[37,38]

Another interesting finding is the increased H3K4me3 gains on developmental transcription factors, such as *FOXP1* and *FOXA2*, in MCI or AD. These factors are typically active during neurodevelopment but become repressed in mature neurons.[33,39] Their reactivation in MCI and AD implies the possible emergence of neuronal dedifferentiation program to induce less precise neural representations, an age-related process linked to cognitive decline.[40,41]

In this study, we revealed the alterations of histone methylation at gene promoters in AD, while prior studies

Table 1. Summary of histone methylation changes during progression from MCI to AD.

Module/Category	Histone modification pattern (promoters)	Key representative genes	Main functions/Pathways	Stage trend (MCI → AD)	Interpretation/Potential application
Synaptic repression modules	↓ H3K4me3 (loss of activation mark) ↑ H3K27me3 (gain of repression mark)	*CACNG3, GRIA2, NRXN1, SYT1, SHANK2/3, GABRA1, GRIK2, DLG2, SLC6A13, BDNF, NRG1*	Synaptic signaling, vesicle exocytosis, calcium transport, neurotransmitter receptor activity	Repression begins in MCI (H3K27me3 gain), deepens in AD (H3K4me3 loss)	Early synaptic repression signature, potential prodromal biomarker set and target for chromatin reactivation therapies (e.g., PRC2/KDM6 or KMT2A modulation.
Transcriptional activation module	↑ H3K4me3 (gain of activation mark)	*RUNX3, EZH2, OTX2, GATA3, PAX5, HOXA5, SOX7, FOXA2, FOXP1*	Transcriptional control, neurodevelopment, inflammatory signaling	Activation evident in MCI, sustained or amplified in AD	Compensatory or maladaptive activation of regulatory programs; candidate targets for epigenetic normalization (e.g., KDM5/KMT2A axis).
Stage-switch module	H3K4me3 ↑ (MCI) → ↓(AD)	*UGT8, ENPP6, CR1, PTPRK, NLGN1, PCDHB10, LRRC4C*	Cell adhesion, synapse remodeling	H3K4me3 gain in MCI → loss in AD	Transitional chromatin state reflecting progressive loss of activation potential; represents a putative window for therapeutic intervention.

Module-specific alterations in H3K4me3 and H3K27me3 occupancies define a coordinated, stage-dependent chromatin reorganization underlying synaptic loss and transcriptional gain.

have reported thousands of AD-associated histone acetylation alterations at enhancers/promoters.[9–13,28] These two histone modifications differ in enzymology, kinetics, and genomic targeting. At synaptic genes, compared to previous findings on the elevation of HDAC2 in AD,[10] our finding on H3K4me3 losses and H3K27me3 gains in MCI and AD provided an additional layer of regulation. At transcription factors, our finding on H3K4me3 gains also complemented the previous finding of H3K9ac and H3K27ac gains in AD.[9]

The observed greater loss of permissive H3K4me3 at synaptic genes in AD compared to MCI, and conversely, the more pronounced gain of repressive H3K27me3 in MCI compared to AD, likely reflect distinct stages of epigenetic and neuronal adaptation during disease progression. Early in disease (MCI), the enhanced deposition of H3K27me3 at synaptic gene promoters may represent an actively regulated neuronal stress response, serving as a potentially reversible epigenetic mechanism aimed at transiently reducing synaptic load and metabolic demands. As pathology advances into AD, persistent neuronal insults, such as chronic inflammation, amyloid accumulation, and tau pathology, may overwhelm these protective mechanisms, resulting in permanent chromatin remodeling marked by pronounced loss of H3K4me3. Consequently, the severe reduction of permissive H3K4me3 on synaptic genes in AD likely indicates irreversible transcriptional dysfunction, reflecting advanced neuronal and synaptic deterioration characteristic of late-stage neurodegeneration.

Our observation that histone methylation alterations occur in a disease stage-dependent manner highlights the complexity of chromatin remodeling in AD progression. WGCNA analyses emphasize the nuanced epigenetic dynamics: some modules showed H3K4me3 losses or gains throughout disease progression (e.g., MEgrey60 and MEyellow), whereas some modules had H3K4me3 gains in MCI but losses in AD (e.g., MEgreenyellow). Such dynamic chromatin state changes likely reflect evolving responses to neuronal stress and shifting transcriptional programs as degenerative signals proceed.[9,11]

Given the mechanistic significance of histone modifications, targeting dysregulated chromatin states could represent a novel therapeutic avenue. In agreement with this, pharmacological manipulation of epigenetic enzymes to normalize histone methylation (H3K4me3 and H3K9me2) levels ameliorated cognitive and synaptic deficits in mouse models of AD.[42–45]

This study has several limitations. First, because of the small sample size and big variations of ChIP-seq data, a rather low threshold was selected in the analysis. More stringent analyses could be performed when more samples become available. Second, all data analyzed were from females due to insufficient male samples, so it awaits to be tested whether comparable results also occur in males. Nevertheless, the predominance of female donors in the available data reflects AD being more prevalent in women compared to men.[46] Another limitation is that all chromatin profiles were generated from bulk dorsolateral prefrontal cortex, which lacks cell-type resolution. Some disease-associated changes could reflect shifts in cellular composition rather than locus-specific regulation. Without sorted nuclei or single-cell assays, it is difficult to fully distinguish these effects.

In summary, our comprehensive profiling of histone methylation dynamics highlights critical stage-dependent epigenetic reorganization events influencing synaptic dysfunction and transcriptional responses in MCI and AD (Table 1). Our findings, synergizing with recent literature, reinforce the importance of histone modification changes in neurodegenerative progression and open novel therapeutic strategies targeting chromatin dysregulation at early stages of disease. In future studies, we intend to build upon the findings to explore epigenetics-based treatment strategy for AD. For example, we will examine whether the increased expression of key transcriptional regulators represents a compensatory response to neurodegenerative stress or a causal factor for gene dysregulation in AD. We will find out whether the identified gene hits can be used as plausible markers for AD or MCI. We will also examine whether inhibiting H3K27me3 methyltransferase *EZH2* at the early stage of AD could mitigate the over-repression of synaptic genes and slow down the functional loss.

Acknowledgements

We thank the University at Buffalo's Center for Computational Research for providing computational infrastructure to run our software.

ORCID iDs

Prachetas Jai Patel https://orcid.org/0000-0002-5895-5905
Zhen Yan https://orcid.org/0000-0002-3519-9596

Ethical considerations

Not applicable

Consent to participate

Not applicable

Consent for publication

Not applicable

Author contribution(s)

Prachetas Jai Patel: Data curation; Formal analysis; Methodology; Validation; Visualization; Writing – original draft.

Zhen Yan: Conceptualization; Funding acquisition; Project administration; Resources; Supervision; Writing – review & editing.

Funding

The authors disclosed receipt of the following financial support for the research, authorship, and/or publication of this article: This work is supported by grants from National Institute on Aging (NIH) (grant numbers R01-AG064656 and R01-AG067597) and VA Western New York Healthcare System (grant number I01-BX006357) to Z.Y.

Declaration of conflicting interests

The authors declared no potential conflicts of interest with respect to the research, authorship, and/or publication of this article.

Data availability statement

ChIP-seq data was acquired from ENCODE Project Consortium. Experiment accession numbers are included in Supplemental Table 1. RNA-seq data were acquired from Mount Sinai Brain Bank (MSBB)[47] and Mayo Clinic[48] and the analysis from the Harmonization Study (Synapse IDs: syn3159438, syn5550404, syn9702085). Microarray data was acquired from Icahn School of Medicine at Mount Sinai's microarray study[49] (Gene Expression Omnibus (GEO) accession number: GSE44772). Metadata, processed ChIP-seq data and WGCNA module data have been deposited to GEO (GEO accession number: GSE304086).

Supplemental material

Supplemental material for this article is available online.

References

1. Karran E and De Strooper B. The amyloid hypothesis in Alzheimer disease: new insights from new therapeutics. *Nat Rev Drug Discov* 2022; 21: 306–318.
2. Wilson DM 3rd, Cookson MR, Van Den Bosch L, et al. Hallmarks of neurodegenerative diseases. *Cell* 2023; 186: 693–714.
3. López-Otín C, Blasco MA, Partridge L, et al. Hallmarks of aging: an expanding universe. *Cell* 2023; 186: 243–278.
4. Lardenoije R, Iatrou A, Kenis G, et al. The epigenetics of aging and neurodegeneration. *Prog Neurobiol* 2015; 131: 21–64.
5. Berson A, Nativio R, Berger SL, et al. Epigenetic regulation in neurodegenerative diseases. *Trends Neurosci* 2018; 41: 587–598.
6. Santana DA, Smith MAC and Chen ES. Histone modifications in Alzheimer's disease. *Genes (Basel)* 2023; 14: 347.
7. Kouzarides T. Chromatin modifications and their function. *Cell* 2007; 128: 693–705.
8. Smith E and Shilatifard A. The chromatin signaling pathway: diverse mechanisms of recruitment of histone-modifying enzymes and varied biological outcomes. *Mol Cell* 2010; 40: 689–701.

9. Nativio R, Lan Y, Donahue G, et al. An integrated multi-omics approach identifies epigenetic alterations associated with Alzheimer's disease. *Nat Genet* 2020; 52: 1024–1035.
10. Gräff J, Rei D, Guan JS, et al. An epigenetic blockade of cognitive functions in the neurodegenerating brain. *Nature* 2012; 483: 222–226.
11. Klein H-U, McCabe C, Gjoneska E, et al. Epigenome-wide study uncovers large-scale changes in histone acetylation driven by tau pathology in aging and Alzheimer's human brains. *Nat Neurosci* 2019; 22: 37–46.
12. Marzi SJ, Leung SK, Ribarska T, et al. A histone acetylome-wide association study of Alzheimer's disease identifies disease-associated H3K27ac differences in the entorhinal cortex. *Nat Neurosci* 2018; 21: 1618–1627.
13. Nativio R, Donahue G, Berson A, et al. Dysregulation of the epigenetic landscape of normal aging in Alzheimer's disease. *Nat Neurosci* 2018; 21: 497–505.
14. Cai Y, Zhang Y, Loh YP, et al. H3K27me3-rich genomic regions can function as silencers to repress gene expression via chromatin interactions. *Nat Commun* 2021; 12: 719.
15. Wang H, Fan Z, Shliaha PV, et al. H3k4me3 regulates RNA polymerase II promoter-proximal pause-release. *Nature* 2023; 615: 339–348.
16. Morris JC, Storandt M, Miller JP, et al. Mild cognitive impairment represents early-stage Alzheimer disease. *Arch Neurol* 2001; 58: 397–405.
17. Dunham I, Kundaje A, Aldred SF, et al. An integrated encyclopedia of DNA elements in the human genome. *Nature* 2012; 489: 57–74.
18. Luo Y, Hitz BC, Gabdank I, et al. New developments on the Encyclopedia of DNA Elements (ENCODE) data portal. *Nucleic Acids Res* 2020; 48: D882–d889.
19. Robinson MD, McCarthy DJ and Smyth GK. Edger: a Bioconductor package for differential expression analysis of digital gene expression data. *Bioinformatics* 2010; 26: 139–140.
20. Ross-Innes CS, Stark R, Teschendorff AE, et al. Differential oestrogen receptor binding is associated with clinical outcome in breast cancer. *Nature* 2012; 481: 389–393.
21. Chen EY, Tan CM, Kou Y, et al. Enrichr: interactive and collaborative HTML5 gene list enrichment analysis tool. *BMC Bioinformatics* 2013; 14: 128.
22. Szklarczyk D, Gable AL, Nastou KC, et al. The STRING database in 2021: customizable protein–protein networks, and functional characterization of user-uploaded gene/measurement sets. *Nucleic Acids Res* 2021; 49: D605–D612.
23. Shannon P, Markiel A, Ozier O, et al. Cytoscape: a software environment for integrated models of biomolecular interaction networks. *Genome Res* 2003; 13: 2498–2504.
24. Langfelder P and Horvath S. WGCNA: an R package for weighted correlation network analysis. *BMC Bioinformatics* 2008; 9: 559.
25. Selkoe DJ. Alzheimer's disease is a synaptic failure. *Science* 2002; 298: 789–791.
26. Terry RD, Masliah E, Salmon DP, et al. Physical basis of cognitive alterations in Alzheimer's disease: synapse loss is the major correlate of cognitive impairment. *Ann Neurol* 1991; 30: 572–580.
27. ST D and Scheff SW. Synapse loss in frontal cortex biopsies in Alzheimer's disease: correlation with cognitive severity. *Ann Neurol* 1990; 27: 457–464.
28. Gräff J and Tsai L-H. Histone acetylation: molecular mnemonics on the chromatin. *Nat Rev Neurosci* 2013; 14: 97–111.
29. Peixoto L and Abel T. The role of histone acetylation in memory formation and cognitive impairments. *Neuropsychopharmacology* 2013; 38: 62–76.
30. Simms BA and Zamponi GW. Neuronal voltage-gated calcium channels: structure, function, and dysfunction. *Neuron* 2014; 82: 24–45.
31. Seoane A, Massey PV, Keen H, et al. L-type voltage-dependent calcium channel antagonists impair perirhinal long-term recognition memory and plasticity processes. *J Neurosci* 2009; 29: 9534.
32. Persico G, Casciaro F, Amatori S, et al. Histone H3 lysine 4 and 27 trimethylation landscape of human Alzheimer's disease. *Cells* 2022; 11: 734.
33. Caldwell AB, Liu Q, Schroth GP, et al. Dedifferentiation and neuronal repression define familial Alzheimer's disease. *Sci Adv* 2020; 6: eaba5933.
34. Yagi R, Junttila IS, Wei G, et al. The transcription factor GATA3 actively represses RUNX3 protein-regulated production of interferon-γ. *Immunity* 2010; 32: 507–517.
35. Levanon D, Bettoun D, Harris-Cerruti C, et al. The Runx3 transcription factor regulates development and survival of TrkC dorsal root ganglia neurons. *EMBO J* 2002; 21: 3454–3463-3463.
36. Tsarovina K, Reiff T, Stubbusch J, et al. The Gata3 transcription factor is required for the survival of embryonic and adult sympathetic neurons. *J Neurosci* 2010; 30: 10833.
37. Tay LS, Krishnan V, Sankar H, et al. RUNX Poly(ADP-ribosyl)ation and BLM interaction facilitate the fanconi anemia pathway of DNA repair. *Cell Rep* 2018; 24: 1747–1755.
38. Dutta B and Osato M. The RUNX family, a novel multifaceted guardian of the genome. *Cells* 2023; 12: 255.
39. Ortiz A, Ayhan F, Khandelwal N, et al. Cell-type-specific roles of FOXP1 in the excitatory neuronal lineage during early neocortical murine development. *Cell Rep* 2025; 44: 115384.
40. Koen JD and Rugg MD. Neural dedifferentiation in the aging brain. *Trends Cogn Sci* 2019; 23: 547–559.
41. Koen JD, Srokova S and Rugg MD. Age-related neural dedifferentiation and cognition. *Curr Opin Behav Sci* 2020; 32: 7–14.
42. Cao Q, Wang W, Williams JB, et al. Targeting histone K4 trimethylation for treatment of cognitive and synaptic deficits in mouse models of Alzheimer's disease. *Sci Adv* 2020; 6: eabc8096.

43. Wang W, Cao Q, Tan T, et al. Epigenetic treatment of behavioral and physiological deficits in a tauopathy mouse model. *Aging Cell* 2021; 20: e13456.
44. Williams JB, Cao Q, Wang W, et al. Inhibition of histone methyltransferase Smyd3 rescues NMDAR and cognitive deficits in a tauopathy mouse model. *Nat Commun* 2023; 14: 91.
45. Zheng Y, Liu A, Wang ZJ, et al. Inhibition of EHMT1/2 rescues synaptic and cognitive functions for Alzheimer's disease. *Brain* 2019; 142: 787–807.
46. Alzheimer's Association. 2025 Alzheimer's disease facts and figures. *Alzheimers Dement* 2025; 21: e70235.
47. Wang M, Beckmann ND, Roussos P, et al. The Mount Sinai cohort of large-scale genomic, transcriptomic and proteomic data in Alzheimer's disease. *Sci Data* 2018; 5: 180185.
48. Allen M, Carrasquillo MM, Funk C, et al. Human whole genome genotype and transcriptome data for Alzheimer's and other neurodegenerative diseases. *Sci Data* 2016; 3: 160089.
49. Zhang B, Gaiteri C, Bodea L-G, et al. Integrated systems approach identifies genetic nodes and networks in late-onset Alzheimer's disease. *Cell* 2013; 153: 707–720.